

Article

Oxidized Graphitic-C₃N₄ with an Extended π -System for Enhanced Photoelectrochemical Property and Behavior

Yue Chang ^{1,2,3,*} , Zhongkui Dai ¹, Kaili Suo ¹, Yuhang Wang ¹  and Xiaona Ren ^{4,*} 

¹ Institute for Advanced Materials and Technology, University of Science and Technology Beijing, Beijing 100083, China

² National Materials Corrosion and Protection Data Center, University of Science and Technology Beijing, Beijing 100083, China

³ BRI Southeast Asia Network for Corrosion and Protection (MOE), Shunde Innovation School, University of Science and Technology Beijing, Foshan 528399, China

⁴ Institute of Powder Metallurgy and Advanced Ceramics, School of Materials and Engineering, University of Science and Technology Beijing, Beijing 100083, China

* Correspondence: changyue@ustb.edu.cn (Y.C.); renxn@ustb.edu.cn (X.R.)

Abstract: In this work, an oxidized g-C₃N₄ film was successfully synthesized using a two-step acid treatment and electrophoretic deposition method. The delocalized π -system of the oxidized g-C₃N₄ film was extended via an annealing treatment. We investigated the influence of hydrogen bonding reversibility and the oxidation treatment of g-C₃N₄ on the photoelectrochemical property and photocathodic protection for 304 stainless steel (304 SS). The resulting oxidized g-C₃N₄ photoelectrode with an extended π -system presents a remarkably enhanced photogenerated electron transfer capability from the photoelectrode to 304 SS (photoinduced OCP negative shift of -0.55 V_{AgCl}) compared with oxidized g-C₃N₄ and protonated g-C₃N₄. The oxidation of g-C₃N₄ facilitates the formation of a porous structure and the introduction of abundant oxygen functional groups, which could promote the effective separation and transport of photogenerated electron-hole pairs. The hydrogen bonding reversibility contributes to the extension of the delocalized π -conjugation system, which could enhance light absorption efficiency. Meanwhile, the annealing treatment is beneficial for prolonging the lifetime of photoelectrons, which could reduce the recombination rate of charge carriers. In addition, to understand how the oxidation treatment and annealing treatment affect the charge transfer behavior, the electronic band structure was investigated, and we found that the oxidized g-C₃N₄ film with an extended π -system possesses a more negative conduction band position, which could reduce the energy barrier of the photogenerated electron transfer.

Keywords: photoelectrochemical property; photocathodic protection; oxidized g-C₃N₄; extended π -system; 304 stainless steel



check for updates

Citation: Chang, Y.; Dai, Z.; Suo, K.; Wang, Y.; Ren, X. Oxidized Graphitic-C₃N₄ with an Extended π -System for Enhanced Photoelectrochemical Property and Behavior. *Crystals* **2023**, *13*, 1386. <https://doi.org/10.3390/cryst13091386>

Academic Editor: Petros Koutsoukos

Received: 24 August 2023

Revised: 13 September 2023

Accepted: 16 September 2023

Published: 18 September 2023



Copyright: © 2023 by the authors. Licensee MDPI, Basel, Switzerland. This article is an open access article distributed under the terms and conditions of the Creative Commons Attribution (CC BY) license (<https://creativecommons.org/licenses/by/4.0/>).

1. Introduction

Photocatalysis is regarded as a promising green and sustainable technology for the solution to the issues of the energy crisis and environmental pollution [1–3]. Photocathodic protection applied in the corrosion of metals is one of the important research branches in photocatalysis. It can utilize renewable solar energy to realize the protection of metallic materials through the transfer of the photo-generated electrons provided by semiconductor photocatalysts to metals. Because of the solar energy without cost and the photocatalysts without consumption in the protection process, it is an ideal economically and environmentally friendly anticorrosion technology, possessing great potential for future development and application. There has thus been significant effort devoted to the development of highly efficient catalysts for the photoelectrochemical protection of metals [4–6].

As a typical metal-free organic semiconductor, graphitic carbon nitride (g-C₃N₄) has gained wide attention as a potential photocatalyst because of its appropriate electronic

structure, suitable band gap (ca. 2.7 eV) for solar light utilization, chemical and thermal stability, and low cost [7–9]. Especially in the photocathodic protection of metals, the negative conduction band level of g-C₃N₄ makes it easier to improve the energy barrier between the semiconductors and the protected metals [10–12]. However, the photocathodic protection performance of pristine g-C₃N₄ still requires improvement, due to the low light absorption and the poor charge transport and separation. In order to address these problems, a number of efforts have been made to modify g-C₃N₄. Zhang et al. [13] reported the synthesis of g-C₃N₄ homojunction films and found that constructing a homojunction contributes to enhanced charge separation, promoting the photocathodic protection of 316 stainless steel and Q235 carbon steel. Jing et al. [14] developed a K and I co-doped g-C₃N₄ photoelectrode for the photoelectrochemical cathodic protection of 316 L stainless steel, proving the important role of K doping modulating the band structure of g-C₃N₄ and promoting the charge transfer. Ma et al. [11] successfully constructed a Fe₂O₃/g-C₃N₄ anti-corrosion coating via conductive adhesive, exhibiting unidirectional electron transport from g-C₃N₄ to the metal matrix and excellent photocathodic protection performance. Furthermore, in recent years, oxidized g-C₃N₄, characterized by an enlarged surface area and electron-rich states, has attracted research interest in the photocatalysis field [15–18]. It has been proved that the oxidation of g-C₃N₄ could remarkably improve photocatalytic activity. Yang et al. [19] utilized the thermal oxidation method to develop oxidized porous g-C₃N₄ for enhanced photocatalytic hydrogen production. Dao et al. [20] utilized the chemical oxidation of a K₂Cr₂O₇/H₂SO₄ mixture to prepare an oxidized g-C₃N₄ and studied the boosted photocatalytic hydrogen evolution of Pt/oxidized g-C₃N₄. Speltini et al. [21] obtained oxidized g-C₃N₄ via the hot HNO₃ oxidation method for improved photocatalytic H₂ production assisted by aqueous glucose biomass. Despite the merits of oxidized g-C₃N₄ as photocatalysts in degradation and hydrogen production, few studies have focused on oxidized g-C₃N₄, especially oxidized g-C₃N₄ film, for the photocathodic protection of metals. Meanwhile, the underlying influence of hydrogen bonding reversibility and the oxidation treatment of g-C₃N₄ on the charge transfer of photocathodic protection is unclear.

Inspired by the above discussion, in this work, we report an oxidized g-C₃N₄ photoelectrode with an extended π -system to boost the photoelectrochemical property and photocathodic protection for 304 SS. The oxidized g-C₃N₄ film was successfully prepared through HCl protonation, HNO₃ oxidation, and electrophoretic deposition methods. The delocalized π -system of the oxidized g-C₃N₄ was extended through a one-step annealing treatment. The crystalline structures, morphologies, chemical composition, optical properties, and band edge position of the resulting photoelectrodes were investigated. The effects of oxidation treatment and delocalized π -system extension on the photoelectrochemical property and behavior of the g-C₃N₄ film obtained by electrophoretic deposition were studied. The promoting mechanism of the oxidized g-C₃N₄ photoelectrode with an extended π -system in the photocathodic protection of 304 SS was demonstrated.

2. Experimental Section

2.1. Material Preparations

2.1.1. Synthesis of Oxidized g-C₃N₄ Powders

All of the reagents were used without further purification. The deionized water was treated at 100 °C before use.

Firstly, the bulk g-C₃N₄ powders were synthesized according to previous reports [15]. More specifically, mixed powders of 4 g melamine (AR, Sinopharm, Shanghai, China) and 1 g thiourea (AR, Sinopharm, Ltd., Shanghai, China) were calcined under air at 570 °C in a muffle furnace for 4 h with a heating rate of 2 °C/min, and the bulk g-C₃N₄ was obtained and designated as B-CN.

Secondly, 0.1 g of B-CN was dispersed into 200 mL of 0.5 mol/L HCl (36~38%, AR, Sinopharm, Shanghai, China) aqueous solution under ultrasonic treatment for 30 min and then continuously stirred for 2 h. The precipitate was collected by filtration, washed with

deionized water until the pH of the solution reached 7, and dried at 60 °C for 12 h. The protonated $g\text{-C}_3\text{N}_4$ was obtained and designated as P-CN.

Then, 0.1 g of P-CN samples and 10 mL HNO_3 (65~68%, GR, Sinopharm, China) were added to a 50 mL round-bottom flask, stirred at 350 rpm, and refluxed at 80 °C for 2 h. After cooling down to room temperature, the suspension was washed with 0.01 mmol/L NaOH (AR, Sinopharm, China) aqueous solution until the pH of the solution reached 7, followed by washing with deionized water and ethanol (AR, Sinopharm, Shanghai, China) several times and freeze drying for 24 h. Finally, the oxidized $g\text{-C}_3\text{N}_4$ was obtained and designated as OP-CN.

2.1.2. Electrophoretic Deposition of OP-CN Films and Annealing Treatment

Fluorine-doped tin oxide (FTO) conductive glass ($14 \Omega/\text{cm}^2$, Wuhan Lattice Solar, Wuhan, China) was ultrasonically cleaned in acetone (AR, Sinopharm, Shanghai, China), ethanol, and deionized water for 0.5 h sequentially.

The obtained P-CN and OP-CN powders were electrophoretically deposited on the surface of the FTO glass, and the typical electrophoretic procedure was as follows:

First, 40 mg of P-CN (or OP-CN) powders and 10 mg of iodine powder (AR, Aladdin, Shanghai, China) were dispersed into 50 mL of acetone solution under stirring for 1 h to obtain a uniformly dispersed slurry. Electrophoretic deposition was performed on a two-electrode configuration using the slurry as the electrolyte. The FTO glass (10×30 mm) and a platinum plate served as the cathode and anode, respectively, with a distance of 15 mm. The P-CN (or OP-CN) samples were deposited on the conductive surface of FTO at 25 V of applied potential for 5 min. They were further dried in a vacuum at 120 °C for 12 h.

In order to increase the delocalized π -conjugation system of OP-CN, the obtained OP-CN film was annealed at 350 °C for 1 h, and the obtained film on the surface of the FTO substrate was denoted as OP-CN(A). The synthesis conditions for the above three film specimens are listed in Table 1.

Table 1. The synthesis conditions for three film specimens.

Film Specimen	Deposited Colloidal Particles	Film-Forming Method	Post-Processing
P-CN	P-CN powders	Electrophoretic deposition	/
OP-CN	O-CN powders	Electrophoretic deposition	/
OP-CN(A)	O-CN powders	Electrophoretic deposition	Annealing treatment

2.2. Characterization

The X-ray diffraction (XRD) pattern of samples was obtained using a Rigaku SmartLab X-ray diffractometer (Cu $K\alpha$ radiation, Rigaku, Tokyo, Japan) over a 2θ range from 10 to 50°. X-ray photoelectron spectroscopy (XPS, Kratos Axis Ultra DLD spectrometer, Al $K\alpha$ X-ray source, Shimadzu, Kyoto, Japan) was used to determine the surface elemental compositions. The morphology and nanostructure characteristics of the resulting samples were determined using a FEI Tecnai G2 F20 high-resolution transmission electron microscope (TEM, FEI, Oberkochen, Germany) and a ZEISS GeminiSEM 300 field-emission scanning electron microscope (FE-SEM, ZEISS, Oberkochen, Germany). Diffuse UV-Vis absorption (DRS UV-Vis) spectra were obtained using a Shimadzu spectrophotometer (UV-2700 Shimadzu, Kyoto, Japan) with the integral sphere in the range of 300–600 nm. Fourier transform infrared (FT-IR) spectroscopic analysis was carried out using a Thermo Scientific Nicolet iS20 spectrometer (Thermo Fisher Scientific, Waltham, MA, USA).

2.3. Photoelectrochemical Measurements and Photoelectrochemical Cathodic Protection Measurements

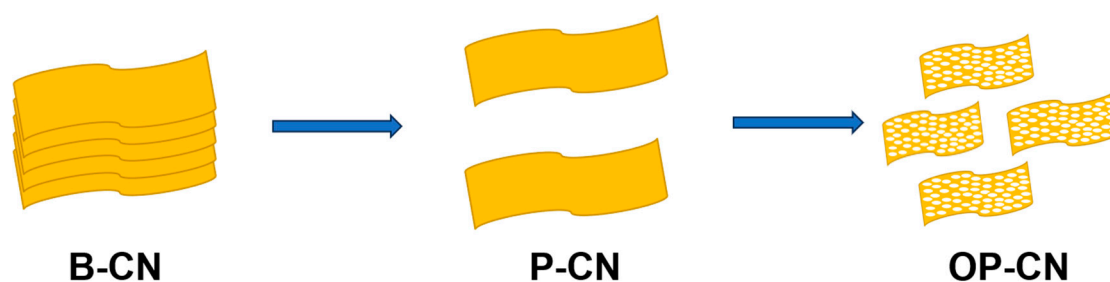
The photoelectrochemical tests and photocathodic protection experiments were performed on a CHI660E electrochemical workstation (CHI, Shanghai, China) in a typical three-electrode configuration. A 300 W Xe lamp (CEL-HXF300, Beijing Perfectlight Technology Co., Ltd., Beijing, China) with an AM 1.5 filter ($100 \text{ mW}/\text{cm}^2$) served as the simulated

solar light irradiation. For the photoelectrochemical tests, 0.5 mol/L NaOH aqueous solution was used as the electrolyte. The prepared film photoelectrode served as the working electrode. A platinum plate ($1 \times 1 \text{ cm}^2$) and an Ag/AgCl electrode were employed as the counter electrode and reference electrode, respectively. The photocurrent density at the open circuit potential was measured under irradiation by a 300 W Xe lamp. EIS measurements were conducted at the open circuit potential over the frequency range of 0.01 to 10^5 Hz under light irradiation. Mott–Schottky data were collected at a scan rate of 50 mV/s with a frequency of 1 kHz. In addition, the photocathodic protection performance of the prepared films was investigated by measuring the OCP curves of the protected 304 SS coupled with the photoelectrode, and the corresponding experimental device is shown in Figure S1, in which the electrolyte of the corrosion cell was 3.5 wt% NaCl solution and that of the photoelectrochemical cell was 0.15 M Na_2S + 0.1 M Na_2SO_3 solution.

3. Results and Discussion

3.1. Characterization of the Oxidized Graphitic Carbon Nitride Powders

The synthesis process for the oxidized $\text{g-C}_3\text{N}_4$ (OP-CN) samples is depicted in Scheme 1. First, the bulk $\text{g-C}_3\text{N}_4$ (B-CN) powders were prepared using a previously reported thermal polymerization method. Subsequently, the yellow bulk powders were exfoliated to obtain the protonated $\text{g-C}_3\text{N}_4$ (P-CN) samples using the HCl acidification–sonication method. Finally, the exfoliated P-CN was oxidized using a strong oxidizing acid (HNO_3) to obtain the oxidized $\text{g-C}_3\text{N}_4$ (OP-CN) sample. The crystal structure of B-CN, P-CN, and OP-CN powders as revealed by X-ray powder diffraction (XRD) characterization is shown in Figure 1. Two diffraction peaks at ca. 12.9° and 27.6° were observed for B-CN, P-CN, and OP-CN, which can be indexed as the typical signals of (100) and (002) of polymeric carbon nitride (JCPDS, 87-1526) [22,23]. Moreover, the intensity of diffraction peaks for P-CN evidently increases compared with that of B-CN, which indicates that the appropriate protonation of HCl can improve the crystallinity of $\text{g-C}_3\text{N}_4$. Protonation to open the edges in the CN framework through broken structural hydrogen bonding could reduce the stacked structure and facilitate the exposure of the lamellar texture [24,25]. However, after HNO_3 pretreatment, the diffraction peaks of OP-CN, especially the extremely low (100) peak, present an obvious decrease. This is attributed to the breakage of the hydrogen bonds in the plane periodicity of the aromatic systems because of the strong oxidative conditions of HNO_3 [26]. It is worth noting that the (002) diffraction peak of OP-CN shows a positive shift of 0.2° from 27.6° to 27.8° , implying a decrease in the interplanar distance owing to the introduction of O atoms and the disturbance of the graphic structure [16]. The electronegativity of added O atoms is stronger than that of the N atoms in the framework, which could strengthen the interactions between the $\text{g-C}_3\text{N}_4$ lamellar texture, leading to the shortening of the interplanar distance. In order to further confirm the presence of oxygen in OP-CN, XPS survey spectra of B-CN, P-CN, and OP-CN samples are provided in Figure 1b. The visible peaks of three elements, C, N, and O, can be found in the survey spectrum of OP-CN, while the survey spectra of B-CN and P-CN samples show an extremely low O peak and two high C and N peaks with similar intensity to that of OP-CN. This feature further confirms the addition of oxygen to $\text{g-C}_3\text{N}_4$ after oxidation treatment, which is in accordance with the results of XRD.



Scheme 1. The synthesis process for oxidized $\text{g-C}_3\text{N}_4$ (OP-CN) samples.

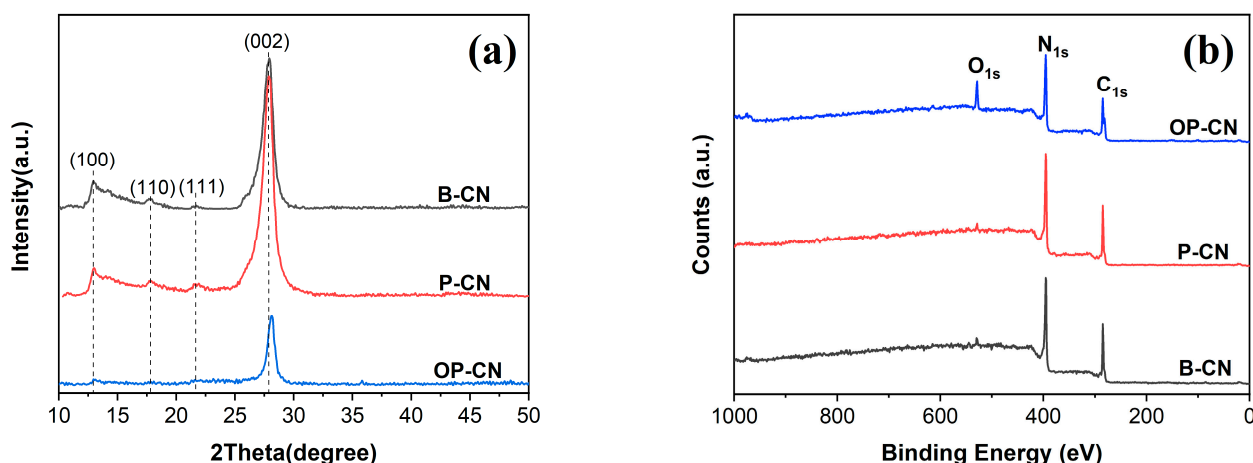


Figure 1. (a) XRD patterns and (b) XPS survey spectra of B-CN, P-CN, and OP-CN powders.

The morphology and nanostructure of B-CN, P-CN, and OP-CN powders were observed using an SEM and a TEM, and the obtained images are shown in Figure 2. It can be seen from Figure 2a,b that both the B-CN and P-CN samples display the typical lamellar stacked structure. Meanwhile, there are more obvious curl edges in P-CN samples because of the exfoliation of the stacked lamellar structure caused by protonation. As shown in Figure 2c, the OP-CN samples exhibit interconnected porous networks in addition to the lamellar texture. Upon close observation, it can be observed that the particle boundaries of the B-CN and P-CN samples are abundant (inset of Figure 2a,b), while those of the OP-CN samples become indistinct (inset of Figure 2c). The TEM image in Figure 2d depicts the morphology of OP-CN. A thin layered structure with a wrinkle shape is observed, where several black strips could correspond to the overlap layers.

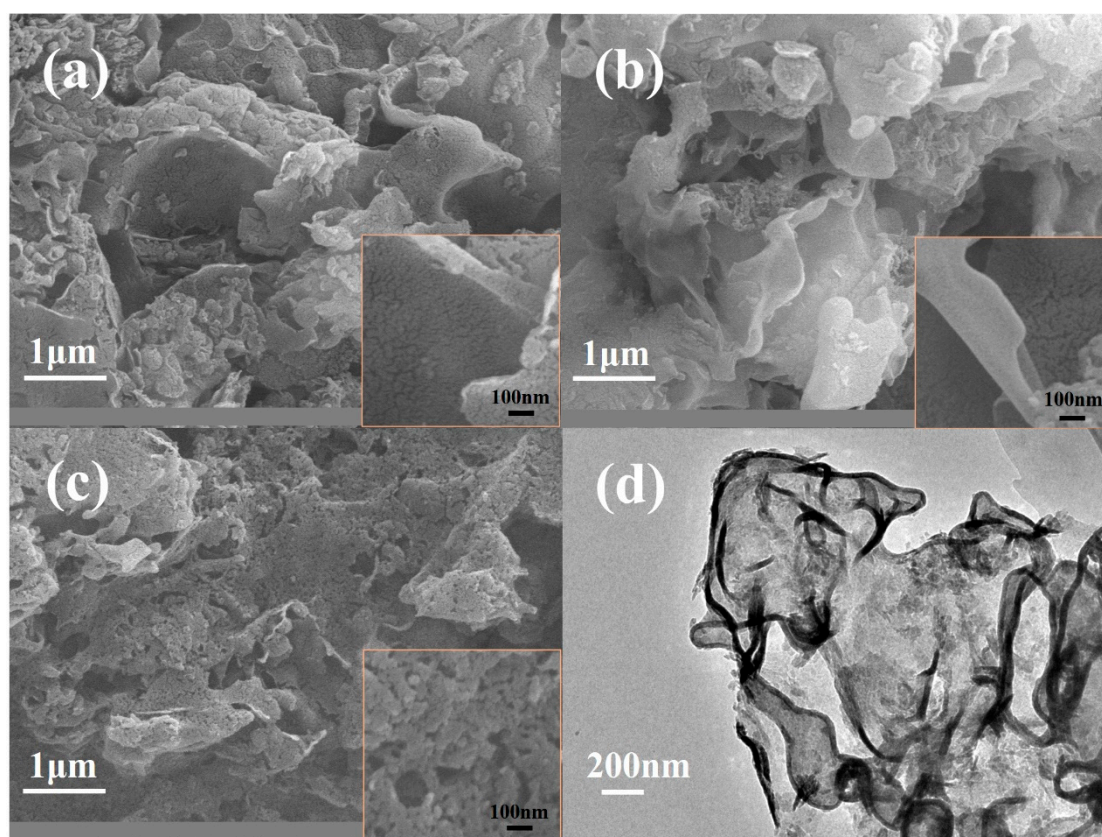


Figure 2. SEM images of (a) B-CN, (b) P-CN, and (c) OP-CN; (d) TEM image of OP-CN.

The DRS UV-Vis spectra of B-CN, P-CN, and OP-CN samples are exhibited in Figure 3. Both the B-CN and P-CN samples present very similar optical absorption in the range of 400–600 nm, and their absorption edges are about 477 nm. This indicates that the HCl moderate protonation of B-CN samples in this work has little effect on the absorption edge, and the electronic band structure could remain largely the same. After oxidation treatment, there is the presence of a semiconductive electronic band structure for the OP-CN samples, but the absorption edge shows an evident blue shift from 477 nm to 446 nm. According to the Tauc plot $((\alpha hv)^{1/2} - hv)$ method (inset of Figure 3a), the band gap energies of three samples can be calculated, in which the E_g values of B-CN and P-CN are both 2.60 eV, while that of OP-CN is 2.78 eV with an increase of 0.18 eV. This increase could be mainly induced by the oxidation of the P-CN frameworks, enabling a partially decreased delocalized π -conjugation system [26,27]. In order to study the effect of HNO₃ oxidation on the structure of carbon nitride frameworks, the B-CN, P-CN, and OP-CN samples were characterized by FT-IR spectra, and the results are shown in Figure 3b. It could be found that the FT-IR spectrum of P-CN is similar to that of B-CN, and there are three typical characteristic peaks at 810 cm⁻¹, 1200–1650 cm⁻¹, and 3000–3360 cm⁻¹, corresponding to the breaking mode of triazine units, the stretching mode of CN heterocycles, and the stretching vibration of N-H or the surface hydroxyl groups. For the OP-CN samples, the breaking vibration at 809 cm⁻¹ for triazine units and the skeletal vibrations at 1200–1650 cm⁻¹ for CN heterocycles are still present, which demonstrates the excellent chemical inertness of the melon units [10,23,28]. Significantly, the intensities of the peak at 1085 cm⁻¹ (belonging to the stretching vibration of C–O), the peak at 1635 cm⁻¹ (belonging to the carboxyl group and carbonyl group), and the peak at 3154 cm⁻¹ (belonging to the hydroxyl functional groups) for OP-CN are stronger than those of P-CN [29,30]. These results indicate that the intrinsic structure of pristine g-C₃N₄ can be preserved but with abundant oxygen functional groups on the edge of CN frameworks after HNO₃ etching, which is in agreement with the results of XRD and XPS.

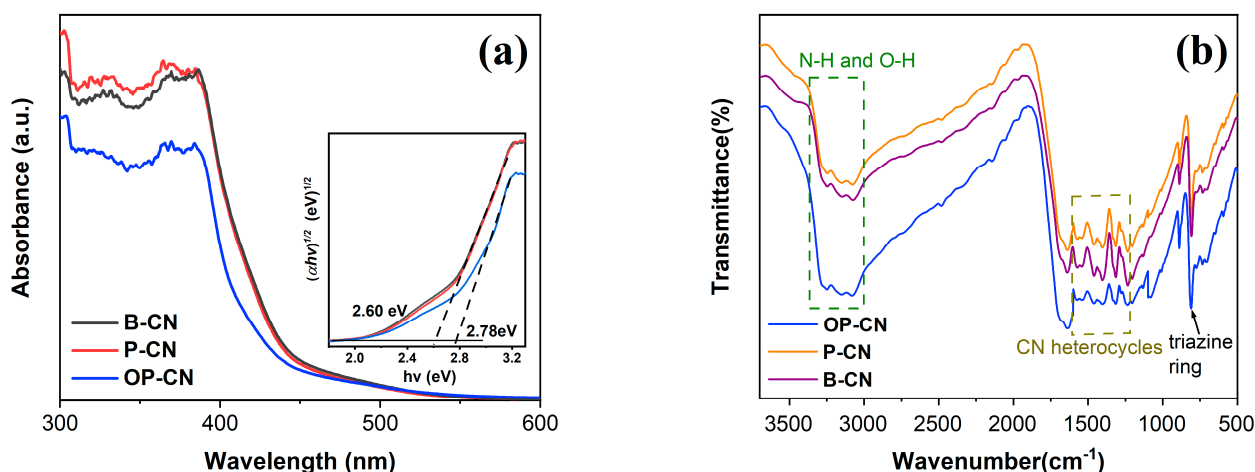


Figure 3. (a) DRS UV-Vis spectra and (b) FT-IR spectra of B-CN, P-CN, and OP-CN powders.

3.2. The Extension of the Delocalized π -Conjugation System for OP-CN Film

It has been discussed and proved that the interfacial hydrogen bonding between the melon units in the frameworks of g-C₃N₄ is disrupted by the strong oxidation of HNO₃, thereby promoting the further depolymerization of g-C₃N₄ to obtain the smaller particles. These smaller particles would facilitate the formation of a uniform film using the electrophoretic method. Meanwhile, the interconnected porous structure after the HNO₃ oxidation treatment would be beneficial for the diffusion and mass transfer in film photoelectrodes. However, according to the results obtained using DRS UV-Vis, the oxidation treatment prompted the blue shift of the light absorption edge for P-CN samples, indicating an enlargement of the band gap and a reduction in the light absorbance range

for the film photoelectrode. This result leads to a low solar energy conversion efficiency of the OP-CN photoelectrode and devalues its photochemical application.

It is worth mentioning that hydrogen bonds have a strong reversibility and can be easily manipulated [31]. The extended π -conjugation system could be re-established through an annealing treatment, thereby narrowing the band gap of OP-CN and improving its light absorption [26].

In order to prove the above discussion, the OP-CN(A) film was prepared through annealing at 350 °C for 1 h. The corresponding crystal structure and optical properties were characterized by XRD and DRS UV-Vis, and the OP-CN film was used as a reference. As shown in Figure 4a, after deducting the characteristic peaks of SnO₂ (JCPDS No. JCPDS No. 41-1445) belonging to the FTO substrate, the data originating from OP-CN(A) film can be well indexed to the diffraction peaks of g-C₃N₄. It is widely accepted that the (002) and (100) peaks derive from the interlayer reflection of a graphite-like structure and the in-plane repeated tri-s-triazine units, respectively. The OP-CN powders (Figure 1) and film (Figure 4) both present an evident (002) peak and an extremely low (100) peak, which implies that the in-plane periodicity of the aromatic systems has been partially destroyed because of the disruption of the hydrogen bonds by HNO₃ treatment. As expected, the (100) peak of OP-CN(A) can be observed compared with OP-CN, suggesting that the OP-CN structure can be recovered to some extent and the extended π -conjugation system can be rebuilt via annealing treatment. In order to further demonstrate the extension of the aromatic π -conjugation system for OP-CN(A) compared with OP-CN, the DRS UV-Vis spectra of OP-CN and OP-CN(A) are exhibited in Figure 4b. The absorption edge of OP-CN(A) is about 475 nm, but there is an obvious red shift from 446 nm to 475 nm compared with OP-CN. This red shift directly indicates that the delocalized π -conjugation system can be extended after annealing treatment [27,32]. The band gap energy of OP-CN(A) can also be estimated as 2.61 eV using the Tauc plot method (inset of Figure 4b).

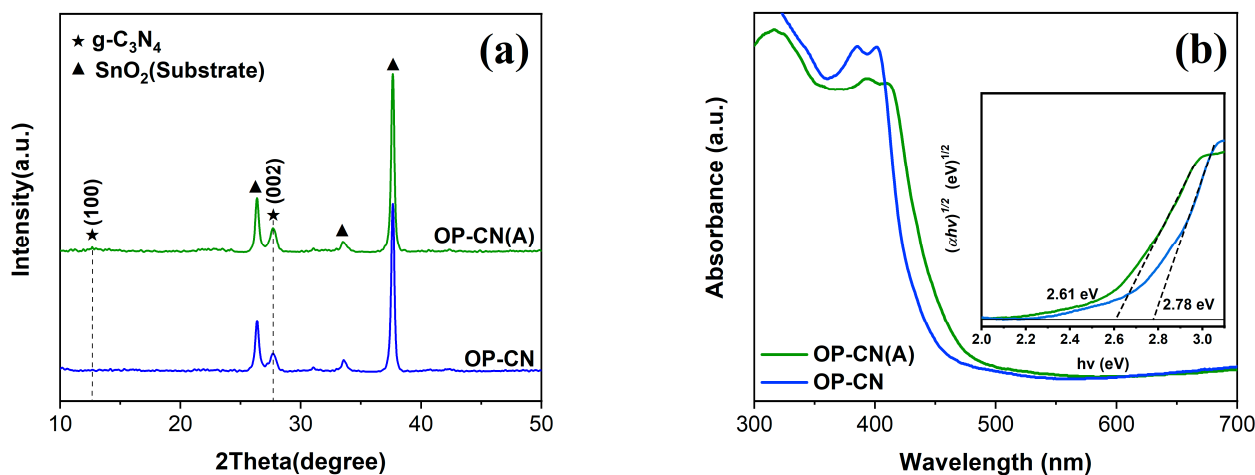


Figure 4. (a) XRD patterns and (b) DRS UV-Vis spectra of OP-CN (before the annealing treatment) and OP-CN(A) (after the annealing treatment) film.

3.3. Photoelectrochemical and Photocathodic Protection Performance of OP-CN with Extended π -Conjugation Systems

The photoelectrochemical performance of P-CN and OP-CN photoelectrodes obtained by electrophoretic deposition and OP-CN(A) photoelectrode obtained by the annealing treatment of OP-CN film was investigated using the transient photocurrent response curve (I-t) and electrochemical impedance spectroscopy (EIS). It can be clearly observed in Figure 5a that three kinds of photoelectrodes show an evidently positive response to light irradiation in the variation in photocurrent density with on/off illumination. The P-CN photoelectrode presents the lowest photocurrent density of 4 $\mu\text{m}/\text{cm}^2$, while the photocurrent density of OP-CN photoelectrode increases to 13 $\mu\text{m}/\text{cm}^2$. The enhancement

of photocurrent density can be explained as follows: On the one hand, there is the formation of the porous structure. The interconnected porous structure facilitates the diffusion and mass transfer of electrolytes, which can consume the photogenerated holes [19]. On the other hand, there is the introduction of abundant oxygen functional groups. The abundant oxygen functional groups favor the enhancement of the local electric field between the surface and bulk of OP-CN, which can promote the transfer of photogenerated electron–hole pairs [30,33]. Thus, although the absorption edge of OP-CN has a blue shift (Figure 3a), which indicates that its band gap becomes large, the photocurrent density of the OP-CN photoelectrode is higher than that of P-CN because of the formation of porous structure and abundant oxygen functional groups. Further, with the annealing treatment of the OP-CN film, the OP-CN(A) photoelectrode shows a significantly enhanced photocurrent density ($48 \mu\text{A}/\text{cm}^2$), which might be mainly attributed to the fact that the extended delocalized π -system decreases the optical gaps.

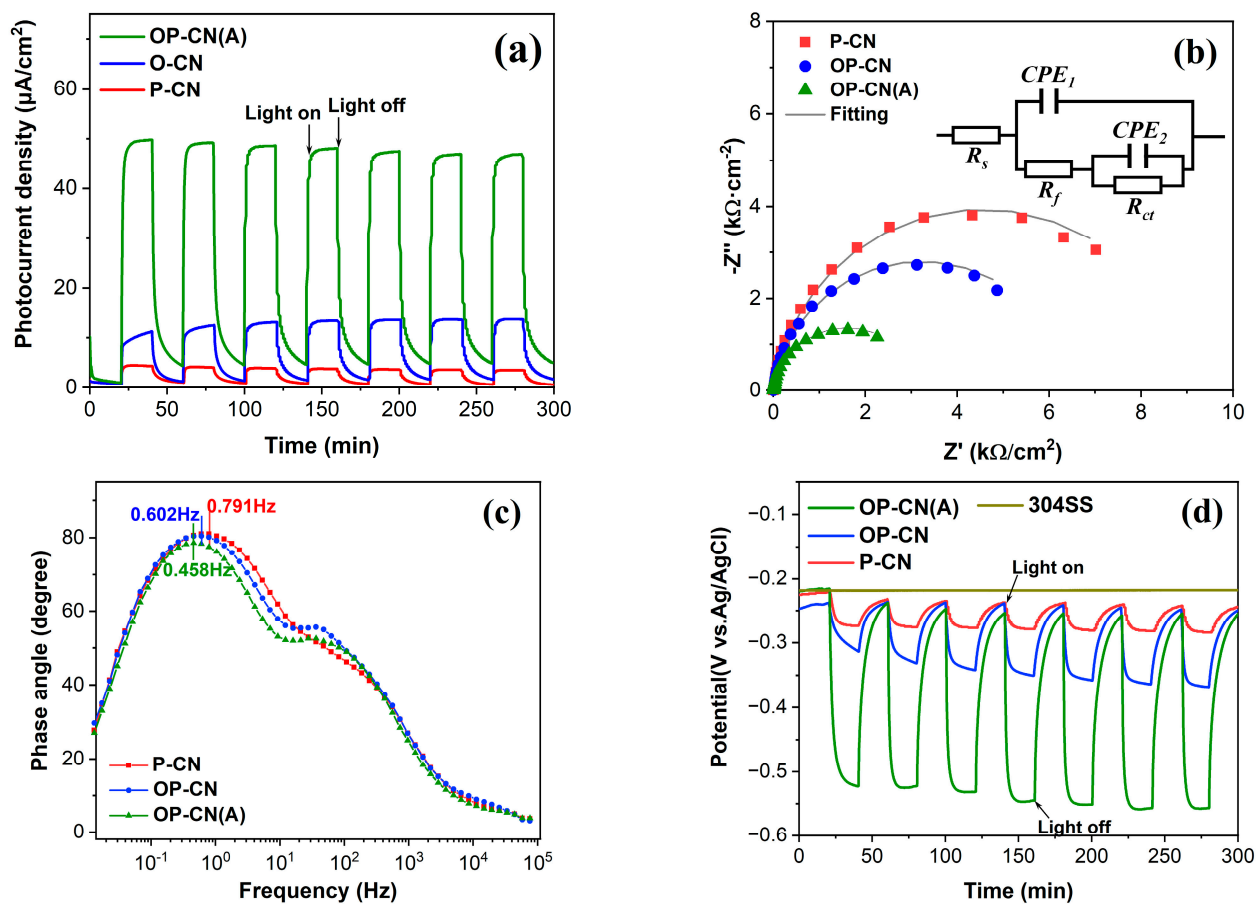


Figure 5. (a) Photocurrent density–time curves, (b) Nyquist plots, and (c) Bode phase angle plots of the prepared photoelectrodes including P-CN, OP-CN, and OP-CN(A) under light irradiation; (d) photoinduced OCP–time curves of P-CN, OP-CN, and OP-CN(A) photoelectrodes coupled with 304 SS under light irradiation, and the OPC curve of bare 304 SS.

In order to study charge transfer behaviors under illumination, EIS measurements were carried out at an open circuit voltage under light irradiation. The Nyquist plots and Bode phase angle plots are given in Figure 5b,c. The inset in the Nyquist plots exhibits the equivalent circuit model with a two-time constant used for the plot fitting, and the fitting data are listed in Table 2. In the equivalent circuit of the Nyquist plots [34,35], R_s represents the series resistance, R_f refers to the film resistance, R_{ct} is the charge transfer resistance, and CPE_1 and CPE_2 represent the constant phase elements. The constant phase element (CPE) can be expressed by the equation $CPE = \frac{1}{Y_0(j\omega)^n}$, where Y_0 and n represent the admittance

magnitude of the CPE and the exponential term ($0 < n \leq 1$), respectively; ω is the angular frequency in rad s^{-1} ($\omega = 2\pi f$); and $j^2 = -1$ is an imaginary number [36,37]. The order of charge transfer resistance for the P-CN, OP-CN, and OP-CN(A) photoelectrodes is as follows: OP-CN(A) (3.20 k Ω) < OP-CN (6.48 k Ω) < P-CN (9.14 k Ω). The R_{ct} value of the OP-CN(A) photoelectrode is significantly reduced compared with those of the OP-CN and P-CN photoelectrodes. This indicates that HNO₃ oxidation can enhance charge carrier transport in g-C₃N₄, and the subsequent annealing treatment further decreases the defect centers for charge recombination, which is in agreement with the results of the above photocurrent–time tests.

Table 2. The equivalent circuit model EIS results for different samples.

Sample	R_s (Ω)	CPE_1, Y_0 (S·sec ^{n})	n_1 ($0 < n_1 \leq 1$)	R_f (Ω)	CPE_2, Y_0 (S·sec ^{n})	n_2 ($0 < n_2 \leq 1$)	R_{ct} (k Ω)
P-CN	2.47	3.83×10^{-4}	0.847	27.6	3.30×10^{-4}	0.993	9.14
OP-CN	1.67	5.91×10^{-4}	0.8491	31.91	4.76×10^{-4}	1	6.48
OP-CN(A)	1.31	10.3×10^{-4}	0.825	27.1	8.73×10^{-4}	1	3.20

Additionally, the characteristic peaks of the P-CN, OP-CN, and OP-CN(A) photoelectrodes can be observed in Figure 5c in the Bode phase angle plots of the photoelectrodes under illumination. The lifetime of photogenerated electrons (τ) is associated with the frequency value (f_{max}) corresponding to the first characteristic peak, which can be estimated using the equation $\tau = \frac{1}{2\pi f_{max}}$ [35,38]. The calculated τ values of the three photoelectrodes are 201 ms for P-CN, 264 ms for OP-CN, and 348 ms for OP-CN(A). As it is known, the prolonged lifetime of photoelectrons would be beneficial for the efficient separation of photogenerated carriers. The OP-CN(A) photoelectrode shows the longest photoelectron lifetime, indicating that the oxidation and subsequent annealing treatment can reduce the recombination rate of charge carriers. The results of the above EIS and photocurrent response tests can illustrate the OP-CN(A) photoelectrode presents the best photoelectrochemical performance compared with P-CN and OP-CN.

The photocathodic protection performance of P-CN, OP-CN, and OP-CN(A) photoelectrode was evaluated by monitoring the variation in photoinduced open circuit potential (OCP). Figure 5d shows the time-dependent curves of OCP with on/off illumination for three photoelectrodes coupled with the 304 SS. The OPC curve of bare 304 SS is about -0.21 V. Three kinds of photoelectrodes all present a sensitivity to light irradiation, and there is a sharp decrease in the photoinduced OCP from the darkness to the illumination, which can be attributed to the photogenerated electrons migrating from the photoelectrode to the coupled 304 SS, polarizing the metals and inducing a negative shift of their corrosion potential. The photoinduced OPC in the fourth cycle is -0.28 V for P-CN, -0.35 V for OP-CN, and -0.55 V for OP-CN(A). It could be found that OP-CN(A) exhibits a more negative shift of the photoinduced potential compared with OP-CN and P-CN. This might be mainly attributed to the enhanced light absorption efficiency and improved photogenerated charge separation efficiency caused by the extended π -system and the optimized morphology and crystal structure, which is consistent with the above results of the characterization analysis and photoelectrochemical performance. Thus, the OP-CN(A) photoelectrode exhibits the best photocathodic protection performance.

3.4. The Promoting Mechanism of OP-CN Photoelectrode with the Extended π -Conjugation Systems

The investigation of the electronic band structure of P-CN, OP-CN, and OP-CN(A) was performed with the combined analysis of the DRS UV-Vis spectra and Mott–Schottky plots. According to the Mott–Schottky relationship, the interface capacitance (C) as a function of electrode potential (V) under depletion conditions was obtained using the equation $\frac{1}{C^2} = \frac{2(V - V_{fb} - kT/e_0)}{\epsilon\epsilon_0 A^2 e_0 N_d}$, in which e_0 is the electronic charge constant (1.6×10^{-19} C); V_{fb} represents the flat band potential; ϵ and ϵ_0 are the relative permittivity constant of g-C₃N₄

and the vacuum permittivity constant (8.86×10^{-14} F/cm), respectively; N_d and A represent the carrier density and area, respectively; and k and T refer to Boltzmann's constant and the absolute temperature, respectively [39]. As shown in Figure 6a, the positive slope in the linear region of the Mott–Schottky plots indicates that three photoelectrodes all present typical n-type semiconductor behavior. The flat band potential (V_{fb}) can be determined through the linear extrapolations with $C^{-2} = 0$, which is -0.92 V_{RHE} for P-CN, -0.91 V_{RHE} for OP-CN, and -0.97 V_{RHE} for P-CN. It is known that the V_{fb} is approximately equal to the conduction band (CB) edge for n-type semiconductors [40]. In addition, the E_g values of P-CN, OP-CN, and OP-CN(A) are 2.60, 2.78, and 2.61 eV, respectively. Thus, the valence band (VB) edge potentials of P-CN, OP-CN, and OP-CN(A) can also be estimated as 1.68, 1.87, and 1.64 V_{RHE}, respectively.

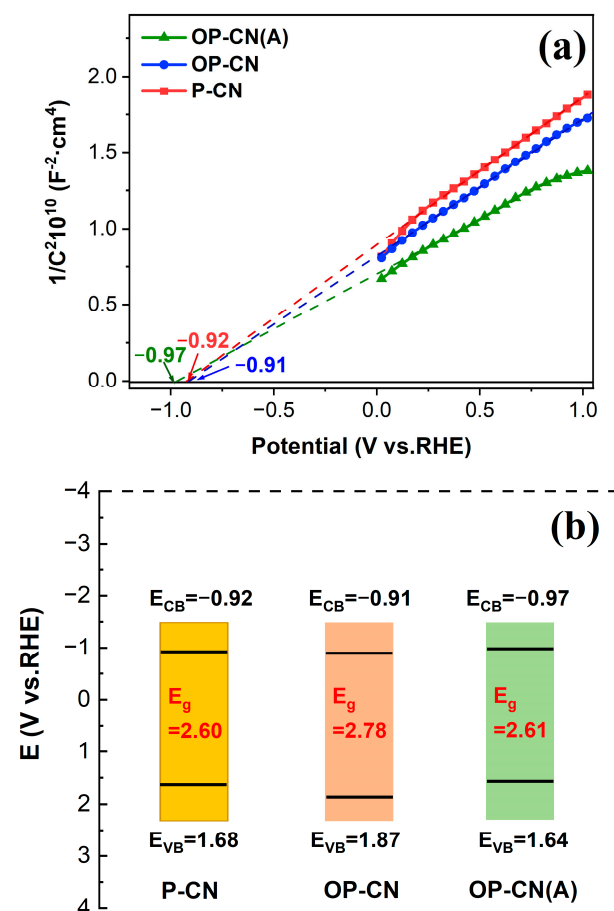


Figure 6. (a) Mott–Schottky plots and (b) the corresponding electronic band structures of P-CN, OP-CN, and OP-CN(A).

Based on the above discussion, a possible promoting mechanism of OP-CN(A) is proposed. The energy band structure of three photoelectrodes is illustrated in Figure 6b. Under light irradiation, OP-CN(A) can be excited, and the electron–hole pairs are generated on the CB and VB of the semiconductors, respectively. The oxidation treatment and annealing treatment cause a change in the electronic band structure of $g\text{-C}_3\text{N}_4$. The extended π -system can narrow the band gap and improve the light absorption; the negative shift of E_{CB} can reduce the energy barrier for photogenerated electron transfer between the photoelectrode and protected metals. The porous structure, abundant oxygen functional groups, and prolonged lifetime of photoelectrons can boost the separation and transfer efficiency of photogenerated electron–hole pairs. In this case, the OP-CN(A) photoelectrode could provide more effective photogenerated electrons for migration to the surface of 304 SS.

Therefore, oxidized g-C₃N₄ with an extended π -system exhibits the best photocathodic protection performance.

4. Conclusions

In summary, we successfully fabricated an oxidized g-C₃N₄ film through a two-step acid treatment and electrophoretic deposition method and subsequently extended the delocalized π -system of oxidized g-C₃N₄ film via an annealing treatment. The resulting samples were characterized by XRD, XPS, SEM, TEM, DRS UV-Vis, and FT-IR. The oxidized g-C₃N₄ film with an extended π -system presents significantly enhanced photoelectrochemical properties and behaviors, as indicated by the photoinduced potential ($-0.55 V_{AgCl}$) coupled with 304 SS. Through the investigation of the charge transfer behavior and electronic band structure, the enhancement of photocathodic protection performance can be attributed to the synergistic effect of the narrow band gap, pull-up conduction band position, abundant oxygen functional groups, and prolonged lifetime of photoelectrons. This synergistic effect could extend the light absorption range, promote the separation efficiency of photogenerated electron–hole pairs, and reduce the charge recombination rate, which contributes to the transport of photogenerated electrons onto the protected metals. This work provides a reference for the potential application of photocathodic protection materials as anodes to inhibit the corrosion of steel.

Supplementary Materials: The following supporting information can be downloaded at: <https://www.mdpi.com/article/10.3390/cryst13091386/s1>, Figure S1: The experimental device of photoinduced OCP.

Author Contributions: Conceptualization, Y.C.; methodology, Y.C. and Z.D.; formal analysis, Z.D. and Y.W.; investigation, Y.C., Z.D. and K.S.; data curation, K.S. and Y.W.; writing—original draft preparation, Y.C.; writing—review and editing, X.R.; supervision, Y.C. and X.R.; project administration, X.R.; funding acquisition, Y.C. All authors have read and agreed to the published version of the manuscript.

Funding: This work was supported by the fund of Guangdong Basic and Applied Basic Research Foundation (2021A1515110741) and fund of Fundamental Research Funds for the Central Universities (Grant No. FRF-GF-19-031B).

Data Availability Statement: Not applicable.

Conflicts of Interest: The authors declare no conflict of interest.

References

1. Xu, F.; Weng, B. Photocatalytic hydrogen production: An overview of new advances in structural tuning strategies. *J. Mater. Chem. A* **2023**, *11*, 4473–4486. [[CrossRef](#)]
2. Samanta, B.; Morales-Garcia, A.; Illas, F.; Goga, N.; Anta, J.A.; Calero, S.; Bieberle-Hutter, A.; Libisch, F.; Munoz-Garcia, A.B.; Pavone, M.; et al. Challenges of modeling nanostructured materials for photocatalytic water splitting. *Chem. Soc. Rev.* **2022**, *51*, 3794–3818. [[CrossRef](#)] [[PubMed](#)]
3. Zhou, P.; Navid, I.A.; Ma, Y.; Xiao, Y.; Wang, P.; Ye, Z.; Zhou, B.; Sun, K.; Mi, Z. Solar-to-hydrogen efficiency of more than 9% in photocatalytic water splitting. *Nature* **2023**, *613*, 66–70. [[CrossRef](#)] [[PubMed](#)]
4. Xu, D.; Liu, Y.; Liu, Y.; Chen, F.; Zhang, C.; Liu, B. A review on recent progress in the development of photoelectrodes for photocathodic protection: Design, properties, and prospects. *Mater. Des.* **2021**, *197*, 109235. [[CrossRef](#)]
5. Momeni, M.M.; Motalebian, M.; Lee, B.K. Photoelectrochemical performance of titania nanotubes codoped by vanadium and chromium for protection of stainless steel: A promising photoanode for continuous protection in the dark. *J. Alloys Compd.* **2023**, *946*, 169429. [[CrossRef](#)]
6. Chen, X.; Zhou, G.; Wang, X.; Xu, H.; Wang, C.; Yao, Q.; Chi, J.; Fu, X.; Wang, Y.; Yin, X.; et al. Progress in semiconductor materials for photocathodic protection: Design strategies and applications in marine corrosion protection. *Chemosphere* **2023**, *323*, 138194. [[CrossRef](#)]
7. Deng, A.; Sun, Y.; Gao, Z.; Yang, S.; Liu, Y.; He, H.; Zhang, J.; Liu, S.; Sun, H.; Wang, S. Internal electric field in carbon nitride-based heterojunctions for photocatalysis. *Nano Energy* **2023**, *108*, 108228. [[CrossRef](#)]
8. Nagella, S.R.; Vijitha, R.; Naidu, B.R.; Rao, K.S.V.K.; Ha, C.S.; Venkateswarlu, K. Benchmarking recent advances in hydrogen production using g-C₃N₄-based photocatalysts. *Nano Energy* **2023**, *111*, 108402. [[CrossRef](#)]
9. Chu, X.; Sathish, C.I.; Yang, J.H.; Guan, X.; Zhang, X.; Qiao, L.; Domen, K.; Wang, S.; Vinu, A.; Yi, J. Strategies for improving the photocatalytic hydrogen evolution reaction of carbon nitride-based catalysts. *Small* **2023**, 2302875. [[CrossRef](#)]

10. Ma, X.; Ma, Z.; Zhang, H.; Lu, D.; Duan, J.; Hou, B. Interfacial Schottky junction of $\text{Ti}_3\text{C}_2\text{T}_x\text{MXene}/\text{g-C}_3\text{N}_4$ for promoting spatial charge separation in photoelectrochemical cathodic protection of steel. *J. Photochem. Photobiol. A-Chem.* **2022**, *426*, 113772. [[CrossRef](#)]
11. Ma, Y.; Wang, H.; Sun, L.; Liu, E.; Fei, G.; Fan, J.; Kang, Y.M. Unidirectional electron transport from graphitic- C_3N_4 for novel remote and long-term photocatalytic anti-corrosion on Q235 carbon steel. *Chem. Eng. J.* **2022**, *429*, 132520. [[CrossRef](#)]
12. Bu, Y.; Ao, J.P. A review on photoelectrochemical cathodic protection semiconductor thin films for metals. *Green Energy Environ.* **2017**, *2*, 331–362. [[CrossRef](#)]
13. Zhang, X.; Chen, G.; Li, W.; Wu, D. Graphitic carbon nitride homojunction films for photocathodic protection of 316 stainless steel and Q235 carbon steel. *J. Electroanal. Chem.* **2020**, *857*, 113703. [[CrossRef](#)]
14. Jing, J.; Chen, Z.; Feng, C.; Sun, M.; Hou, J. Transforming $\text{g-C}_3\text{N}_4$ from amphoteric to n-type semiconductor: The important role of pin type on photoelectrochemical cathodic protection. *J. Alloys Compd.* **2021**, *851*, 156820. [[CrossRef](#)]
15. Ming, L.; Yue, H.; Xu, L.; Chen, F. Hydrothermal synthesis of oxidized $\text{g-C}_3\text{N}_4$ and its regulation of photocatalytic activity. *J. Mater. Chem. A* **2014**, *2*, 19145–19149. [[CrossRef](#)]
16. Li, J.; Shen, B.; Hong, Z.; Lin, B.; Gao, B.; Chen, Y. A facile approach to synthesize novel oxygen-doped $\text{g-C}_3\text{N}_4$ with superior visible-light photoreactivity. *Chem. Commun.* **2012**, *48*, 12017–12019. [[CrossRef](#)]
17. Pisanu, A.; Speltini, A.; Vigani, B.; Ferrari, F.; Mannini, M.; Calisi, N.; Cortigiani, B.; Caneschi, A.; Quadrelli, P.; Profumo, A.; et al. Enhanced hydrogen photogeneration by bulk $\text{g-C}_3\text{N}_4$ through a simple and efficient oxidation route. *Dalton Trans.* **2018**, *47*, 6772–6778. [[CrossRef](#)]
18. Xu, J.; Gao, Q.; Bai, X.; Wang, Z.; Zhu, Y. Enhanced visible-light-induced photocatalytic degradation and disinfection activities of oxidized porous $\text{g-C}_3\text{N}_4$ by loading Ag nanoparticles. *Catal. Today* **2019**, *332*, 227–235. [[CrossRef](#)]
19. Yang, L.; Huang, J.; Shi, L.; Cao, L.; Yu, Q.; Jie, Y.; Fei, J.; Ouyang, H.; Ye, J. A surface modification resultant thermally oxidized porous $\text{g-C}_3\text{N}_4$ with enhanced photocatalytic hydrogen production. *Appl. Catal. B Environ.* **2017**, *204*, 335–345. [[CrossRef](#)]
20. Dao, Q.D.; Nguyen, T.K.A.; Dang, T.T.; Kang, S.G.; Nguyen-Phu, H.; Do, L.T.; Van, V.K.H.; Chung, K.H.; Chung, J.S.; Shin, E.W. Anchoring highly distributed Pt species over oxidized graphitic carbon nitride for photocatalytic hydrogen evolution: The effect of reducing agents. *Appl. Surf. Sci.* **2023**, *609*, 155305.
21. Speltini, A.; Scalabrini, A.; Maraschi, F.; Sturini, M.; Pisanu, A.; Malavasi, L.; Profumo, A. Improved photocatalytic H_2 production assisted by aqueous glucose biomass by oxidized $\text{g-C}_3\text{N}_4$. *Int. J. Hydrogen Energy* **2018**, *43*, 14925–14933. [[CrossRef](#)]
22. Li, Y.P.; He, J.Y.; Wang, X.J.; Zhao, J.; Liu, R.H.; Liu, Y.; Li, F.T. Introduction of crystalline hexagonal- C_3N_4 into $\text{g-C}_3\text{N}_4$ with enhanced charge separation efficiency. *Appl. Surf. Sci.* **2021**, *559*, 149876. [[CrossRef](#)]
23. Liu, Q.; Guo, Y.; Chen, Z.; Zhang, Z.; Fang, X. Constructing a novel ternary $\text{Fe(III)}/\text{graphene}/\text{g-C}_3\text{N}_4$ composite photocatalyst with enhanced visible-light driven photocatalytic activity via interfacial charge transfer effect. *Appl. Catal. B-Environ.* **2016**, *183*, 231–241. [[CrossRef](#)]
24. Zhang, Y.; Thomas, A.; Antonietti, M.; Wang, X. Activation of carbon nitride solids by protonation: Morphology changes, enhanced ionic conductivity, and photoconduction experiments. *J. Am. Chem. Soc.* **2009**, *131*, 50–51. [[CrossRef](#)] [[PubMed](#)]
25. Wei, Y.; Wang, Z.; Su, J.; Guo, L. Metal-Free Flexible Protonated $\text{g-C}_3\text{N}_4$ /carbon gots photoanode for photoelectrochemical water splitting. *Chemelectrochem* **2018**, *5*, 2734–2737. [[CrossRef](#)]
26. Zhang, J.; Zhang, M.; Lin, L.; Wang, X. Sol Processing of Conjugated Carbon Nitride Powders for Thin-Film Fabrication. *Angew. Chem. Int. Ed.* **2015**, *54*, 6297–6301. [[CrossRef](#)]
27. Shi, A.; Li, H.; Yin, S.; Liu, B.; Zhang, J.; Wang, Y. Effect of conjugation degree and delocalized π -system on the photocatalytic activity of single layer $\text{g-C}_3\text{N}_4$. *Appl. Catal. B Environ.* **2017**, *218*, 137–146. [[CrossRef](#)]
28. Cui, M.; Cui, K.; Liu, X.; Shi, J.; Chen, X.; Chen, Y. Synergistic effect of mesoporous graphitic carbon nitride and peroxydisulfate in visible light-induced degradation of atenolol: A combined experimental and theoretical study. *Chem. Eng. J.* **2021**, *412*, 127979. [[CrossRef](#)]
29. Sun, X.; Lei, J.; Jin, Y.; Li, B. Long-Lasting and intense chemiluminescence of luminol triggered by oxidized $\text{g-C}_3\text{N}_4$ nanosheets. *Anal. Chem.* **2020**, *92*, 11860–11868. [[CrossRef](#)]
30. Li, Z.; Meng, X.; Zhang, Z. Fabrication of surface hydroxyl modified $\text{g-C}_3\text{N}_4$ with enhanced photocatalytic oxidation activity. *Catal. Sci. Technol.* **2019**, *9*, 3979–3993. [[CrossRef](#)]
31. Zhou, Z.; Zhang, Y.; Shen, Y.; Liu, S.; Zhang, Y. Molecular engineering of polymeric carbon nitride: Advancing applications from photocatalysis to biosensing and more. *Chem. Soc. Rev.* **2018**, *47*, 2298–2321. [[CrossRef](#)] [[PubMed](#)]
32. Cao, S.; Yu, J. $\text{g-C}_3\text{N}_4$ -Based photocatalysts for hydrogen generation. *J. Phys. Chem. Lett.* **2014**, *5*, 2101–2107. [[CrossRef](#)] [[PubMed](#)]
33. Chang, Y.; Xuan, Y.; Quan, H.; Zhang, H.; Liu, S.; Li, Z.; Yu, K.; Cao, J. Hydrogen treated $\text{Au}/3\text{DOM-TiO}_2$ with promoted photocatalytic efficiency for hydrogen evolution from water splitting. *Chem. Eng. J.* **2020**, *382*, 122869. [[CrossRef](#)]
34. Zhou, Z.; Wang, Y.; Li, L.; Yang, L.; Niu, Y.; Yu, Y.; Guo, Y.; Wu, S. Constructing a full-space internal electric field in a hematite photoanode to facilitate photogenerated-carrier separation and transfer. *J. Mater. Chem. A* **2022**, *10*, 8546–8555. [[CrossRef](#)]
35. Pan, G.; Li, J.; Zhang, G.; Zhan, Y.; Liu, Y. Binder-integrated $\text{Bi}/\text{BiOI}/\text{TiO}_2$ as an anti-chloride corrosion coating for enhanced photocathodic protection of 304 stainless steel in simulated seawater. *J. Alloys Compd.* **2023**, *938*, 168469. [[CrossRef](#)]
36. Li, H.; Wang, X.; Liu, Y.; Hou, B. Ag and SnO_2 co-sensitized TiO_2 photoanodes for protection of 304SS under visible light. *Corros. Sci.* **2014**, *82*, 145–153. [[CrossRef](#)]

37. Motalebian, M.; Momeni, M.M.; Lee, B.K. Novel photoanodes based on (Mo-Cr) co-doped titania nanotube for highly efficient photocathodic protection performance of stainless steel. *Appl. Surf. Sci.* **2023**, *610*, 155091. [[CrossRef](#)]
38. Guan, Z.C.; Hu, J.; Wang, H.-H.; Shi, H.Y.; Wang, H.P.; Wang, X.; Jin, P.; Song, G.L.; Du, R.G. Decoration of rutile TiO₂ nanorod film with g-C₃N₄/SrTiO₃ for efficient photoelectrochemical cathodic protection. *J. Photochem. Photobiol. A Chem.* **2023**, *443*, 114825. [[CrossRef](#)]
39. Li, X.; Wan, J.; Ma, Y.; Zhao, J.R.; Wang, Y. Mesopores octahedron GCNOX/Cu₂O@C inhibited photo-corrosion as an efficient visible-light catalyst derived from oxidized g-C₃N₄/HKUST-1 composite structure. *Appl. Surf. Sci.* **2020**, *510*, 145459. [[CrossRef](#)]
40. Jiang, X.; Sun, M.; Chen, Z.; Jing, J.; Feng, C. High-efficiency photoelectrochemical cathodic protection performance of the TiO₂/AgInSe₂/In₂Se₃ multijunction nanosheet array. *Corros. Sci.* **2020**, *176*, 108901. [[CrossRef](#)]

Disclaimer/Publisher's Note: The statements, opinions and data contained in all publications are solely those of the individual author(s) and contributor(s) and not of MDPI and/or the editor(s). MDPI and/or the editor(s) disclaim responsibility for any injury to people or property resulting from any ideas, methods, instructions or products referred to in the content.